Photoacoustics 10 (2018) 48–53

Contents lists available at ScienceDirect

Photoacoustics

journal homepage: www.elsevier.com/locate/pacs

Research article

Imaging of blood flow and oxygen state with a multi-segment optoacoustic ultrasound array

Elena Merčep[a,b], Xosé Luís Deán-Ben[c], Daniel Razansky[a,c,*]

[a] Faculty of Medicine, Technical University of Munich, Germany
[b] iThera Medical GmbH, Munich, Germany
[c] Institute for Biological and Medical Imaging (IBMI), Helmholtz Center Munich, Neuherberg, Germany

ARTICLE INFO

Article history:
Received 12 January 2018
Received in revised form 3 April 2018
Accepted 23 April 2018
Available online 27 April 2018

Keywords:
Optoacoustic imaging
Ultrasonography
Multimodal imaging
Photoacoustics
Color Doppler

ABSTRACT

Changes in hemodynamic parameters are directly linked to biological function and physiological activity. Characterization of hemodynamics is commonly performed by Doppler ultrasound, which provides accurate measurements of blood flow velocity. Multi-spectral optoacoustic tomography is rapidly undergoing clinical translation fostered by its unique and complementary capacity for label-free mapping of the blood volume and the distribution of oxy- and deoxy-hemoglobin in blood. Here we report on a hybrid optoacoustic and ultrasound imaging approach that enables multi-modal imaging of blood flow and oxygen state using a multi-segment detector array. We further demonstrate rendering of multi-modal pulse-echo ultrasound, multi-spectral optoacoustic tomography, and color Doppler images from carotid artery of a healthy subject.

1. Introduction

Simultaneous measurement of multiple hemodynamic parameters is of high importance for the understanding of tissue function and disease progression. Hemodynamic responses are normally produced in response to physical or organ activity, environmental changes as well as neural activity to guarantee proper oxygen delivery to tissues [1,2]. Majority of cardiac and vascular disorders are similarly related to systemic hemodynamic dysfunction, so that hemodynamic measurements are essential in their timely diagnosis and treatment monitoring [3]. Color Doppler ultrasound (US) has arguably become the gold standard for mapping the distribution of blood flow. Handheld US scanners are extensively employed in the clinics for diagnosing blood clots, defects in heart valves, blockage in arteries and numerous other conditions [4]. Owing to its unique capability for non-invasive label-free mapping of the distribution of oxy- and deoxy-hemoglobin deep in living tissues, multi-spectral optoacoustic tomography (MSOT) has recently found widespread use in preclinical imaging applications [5,6] and is undergoing rapid clinical translation in various point-of-care diagnostic applications, such as melanomas [7,8], inflammatory bowel (Crohn's) disease [9], breast abnormalities [10], thyroid cancer [11,12] or peripheral vascular diseases [13].

Efficient integration between MSOT and US in a hybrid hand-held scanner is expected to further accelerate clinical translation of MSOT and significantly enhance imaging performance of the stand-alone systems by simultaneously delivering their highly complementary contrasts. While a number of possible hybridization approaches have been previously suggested [14–18], such an efficient combination is inherently challenged by the fundamentally different excitation and image formation strategies behind the two modalities. Recently, a hand-held probe based on a multi-segment detector array combining linear and concave segments with different inter-element pitch has been reported [19,20]. The different parts of the array provide optimized performance for each modality, hence enabling accurate multi-modal optoacoustic and pulse-echo US imaging. The linear segment may additionally be exploited for other US modes, such as Doppler US.

Here we adopted the multi-segment array approach in order to achieve multi-modal MSOT, pulse-echo US and color Doppler imaging in a hand-held mode. The experimental performance of the multi-modal approach is further showcased by imaging the carotid artery region of a healthy volunteer, where Doppler US is commonly used for the detection of vascular abnormalities, such as stenosis or intraluminal turbulence [21].

* Corresponding author.
E-mail address: dr@tum.de (D. Razansky).

https://doi.org/10.1016/j.pacs.2018.04.002

2. Methods

2.1. Experimental setup

The main system components used for the acquisition of MSOT and US data have been described elsewhere [19,20]. In short, for the MSOT data acquisition, a pulsed Nd:YAG-pumped optical parameter oscillator (OPO) laser source (InnoLas Laser GmbH, Krailling, Germany) is operated at 25 Hz repetition rate, a peak pulse energy of 25 mJ at 730 nm, and a wavelength in the 680–900 nm range tunable on a pulse-by-pulse basis. The excitation light is guided to the specimen via a custom-made fiber bundle (CeramOptec GmbH, Bonn, Germany) resulting in an incident fluence of <10 mJ/cm^2 at the skin surface for the entire wavelength range of interest, well below the maximum permissible exposure limits recommended by the ANSI standards [22].

The transducer array employed in this study (Imasonic SaS, Voray, France) has nominal Tx/Rx bandwidth of 60% around 7.5 MHz central frequency. It combines segments of linear (L) and concave (C) geometry (Fig. 1a). The L segment consists of 128 elements with 0.25 mm (1.25λ) inter-element pitch while the two C segments each have 64 elements with their individual elements separated by a pitch of 0.6 mm (3λ). The concave segments lie on a 40 mm radius arc and all their elements are cylindrically focused at a distance of 38 mm within the common imaging plane. The elements of the linear segment are focused at 34 mm distance from the active aperture.

The OA signals collected by the array probe were digitized by a custom-made data acquisition system (Falkenstein Mikrosysteme GmbH, Taufkirchen, Germany) at a sampling rate of 40 MS/s. The signals were subsequently transferred to a designated PC station using a 1-Gbit Ethernet connection. Image reconstruction was performed using OpenCL-based GPU code.

Pulse-echo US signal acquisition was performed by four 64-channel PCIe acquisition boards (two transmit and two receive boards) custom-built by S-Sharp Corporation, Taiwan. The acquired signals were transferred to the main motherboard, where CUDA-based image reconstruction on a high-level GPU was performed and the images were ultimately transferred as binary raw data files via Ethernet to the main PC. Switching between OA ("receive-only") and US ("transmit-receive") imaging modes was facilitated through a custom-made programmable multiplexing unit (MUX) connected to the transducer array and controlled via a laser-triggered signal from the OA data acquisition system. Any possible acquisition conflict was avoided by allocating strictly defined non-overlapping time windows for the OA and US data recording and processing [20]. Moreover, frame time-stamping enables clearly differentiating the incoming data streams from the different modalities. Only the latest frames with the closest time stamps are overlaid for the multi-modal representation.

Two basic operation modes were enabled by the acquisition hardware, namely, (1) interleaved MSOT and pulse-echo US by means of synthetic transmit aperture (STA) beamforming or (2) interleaved MSOT and duplex US (color Doppler combined with pulse-echo US) by means of dynamic receive focusing (DRF) beamforming, also known as B-scan mode. Switching between the two modes was performed manually.

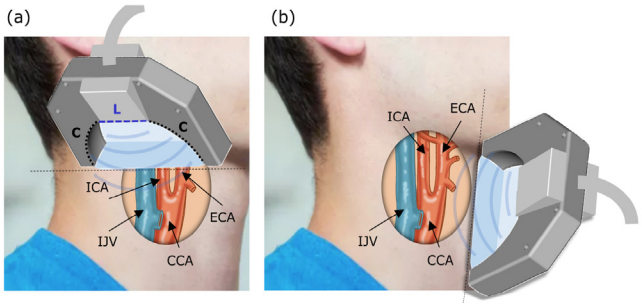

Fig. 1. Geometry of the multi-modal (MSOT, pulse-echo US, and color Doppler) image acquisition with the multi-segment probe in a) transverse and b) longitudinal planes. ICA: internal carotid artery; ECA: external carotid artery; IJV: internal jugular vein; CCA: common carotid artery.

2.2. MSOT imaging

For the MSOT image formation, the optoacoustic signals acquired with all the 256 multi-segment array elements were first pre-processed with a band-pass finite impulse response (FIR) filter (0.05 and 10 MHz cut-off frequencies) and deconvolved with the simulated electrical impulse response of the transducer, obtained using a 2D Gaussian function assuming a detector center frequency of 7.5 MHz, a bandwidth of 60%, and a sampling frequency of 40 MS/s. Two-dimensional OA images were then reconstructed with a standard back-projection algorithm in a field of view (FOV) of 17×30 mm (150 μm pixel size).

For spectral unmixing, the OA images were acquired at seven wavelengths (700, 730, 760, 780, 800, 825, and 850 nm) in order to accurately sample the absorption spectrum profiles of the endogenous chromophores of interest. To minimize the negative effect of motion on the unmixing accuracy, the probe was kept still during acquisition of the multi-wavelength data. Alternatively, motion artefacts in multi-spectral imaging can be effectively averted by using microsecond-delayed triggering of multiple lasers [23], which was however not attempted in the current study. The distributions of oxy- and deoxy-hemoglobin were subsequently rendered by means of spectral fitting of unaveraged single-wavelength images to the known absorption spectra of oxy- and deoxy-hemoglobin [24], and the resulting 2D maps of the specific chromophore distribution were visualized using pseudo-color coding. This type of visualization does not permit quantitative evaluation of blood oxygen saturation but rather intended for visualizing the distribution of oxy- and deoxy-hemoglobin.

2.3. Pulse-echo STA US and duplex US image acquisition

In the pulse-echo US mode, single-cycle 20 Vpp bipolar pulses at 7 MHz frequency were transmitted. The 128 elements of the linear array segment were used for US image formation by employing a synthetic transmit aperture (STA) focusing technique [25]. The concave parts of the array were not considered for US image formation as those would introduce grating-lobe artefacts associated to the large inter-element pitch of the concave segments [20]. The method was realized by sequential pulse transmission from individual elements and detection of the back-scattered echoes with all the array elements. The sampled channels were then stored to build 128 low-resolution images (LRIs) corresponding to each event of an unfocused emission of an ultrasonic pulse from a single element and acquisition of the resulting echoes by all the other elements. The LRIs were formed using delay-and-sum (DAS) beamforming within a FOV of 17×30 mm with a pixel size of 200 μm. The LRIs from subsequent transmit events were coherently summed to form a final high-resolution image (HRI). The LRIs add up at points where the isochronal lines, i.e. those connecting pixels with the same time of flight, overlap on a real scatterer. At other locations, the individual images add incoherently resulting in a much lower signal level. In this way, the STA algorithm synthetically focuses both the transmitted and back-scattered fields throughout the entire image. In our experiments, the synthetically focused beam intervals were set to 200 μm.

In the duplex US imaging mode, a two-dimensional B-scan image was rendered by pulse-echo interrogation of multiple scan lines swept across the FOV using dynamic receive focusing (DRF) type of beamforming. As opposed to STA, in DRF only the back-scattered field is dynamically focused at all points across the FOV while the focus of the transmitted field remains steady [26,27]. Similarly to B-scan pulse-echo image, the color flow map was then generated by multi-gated interrogation of the multiple scan lines using bursts of short US pulses [28]. In this way, many RF back-scattered signals were obtained at multiple sampling sites (gates) along each scan line for a series of emitted US pulses. The group of pulses required to estimate the velocity of blood flow at a particular gate is known as a packet or a pulse train with the time between successive pulse trains determining the effective pulse repetition frequency (PRF) [29]. In our experiments, packet size of 8, PRF of 5 kHz, and 5-cycle 20 Vpp bipolar pulses at 6 MHz frequency was employed. The transmitted field was focused at an approximate depth of 1.5 cm from the tissue surface and the aperture size was varied by means of dynamic apodization [30] to achieve a constant F-number of 2, both in transmit and receive modes. The beam intervals for the color Doppler flow image were set to 300 μm. The frequency shift measured at each gate was automatically correlated using an autocorrelation function and encoded in the image via a preset color scheme with positive Doppler shifts (blood moving towards the transducer) represented by red colors and negative shifts represented by blue colors [31]. The color-coded flow patterns were subsequently superimposed onto the gray-scale anatomical B-scan image [28]. Rendering of two-dimensional 200×200 pixels B-mode US images was performed in real time at a rate of 25 frames per second, while the frame rate in the color Doppler mode was 10 Hz. The latter can be calculated via [32]

$$FPS_{DP} = \frac{1}{\frac{NL_B}{PRF} + \frac{NL_C \cdot PS}{PRF}}, \quad (1)$$

where NL_B is the number of lines in the reconstructed B-mode image; NL_C is the number of lines in the reconstructed color Doppler-mode image; PRF is the pulse repetition frequency [Hz] and PS is the packet size. Clearly, the frame rate can be increased by using larger pixels or, alternatively, by reducing the packet size.

2.4. In vivo imaging

For image acquisition, a healthy volunteer was lying in a supine position with a stretched neck and the chin turned away from the side being examined. For optimal scanning we referred to the standard guidelines for carotid US examinations [33]. The probe was placed on the left side of the lower neck and the scan in the transverse plane was first performed along the common carotid artery slowly moving into the carotid bifurcation area (Fig. 1a). After identifying the internal and external carotid arteries, the probe was kept still to minimize motion artefacts during the MSOT image acquisition. The probe was then slowly rotated 90° and a scan in the longitudinal plane was performed to better visualize the common carotid artery and the bifurcation area (Fig. 2b). All human imaging experiments were done in full accordance with the work safety regulations and guidelines on the safe use of pulsed lasers [34].

3. Results

First, a series of images from the region of the left lower neck were collected in the first operation mode of interleaved MSOT and pulse-echo STA US, as shown in Fig. 2. The OA image acquired at a wavelength of 800 nm (Fig. 2a), which effectively reflects the total hemoglobin contrast, readily allows for the identification of major

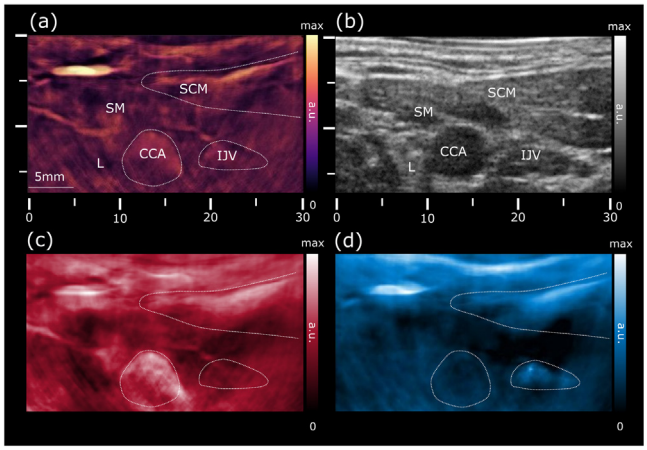

Fig. 2. Cross-sectional views of the left common carotid artery in the transverse plane. (a) Optoacoustic image at 800 nm shows increased vascularization of the skin, strap and sternocleidomastoid muscles, allowing for a clear identification of the common carotid artery and internal jugular vein. (b) Ultrasound pulse-echo STA image revealing the common carotid artery and jugular vein as echo-free structures. (c) Map of the unmixed distribution of oxygenated hemoglobin (HbO_2). (d) The corresponding map of deoxygenated hemoglobin (Hb). CCA: common carotid artery; SCM: sternocleidomastoid muscle; SM: strap muscle; IJV: internal jugular vein; L: thyroid lobe.

blood vessels, such as the common carotid artery and the internal jugular vein owing to their increased blood absorption contrast and characteristic shapes. Note that the same vessels appear hypoechoic in the pulse-echo US image (Fig. 2b). The jugular vein usually appears in a collapsed condition while moderate pressures applied during imaging may have caused additional flattening of the vein. From the US image it is further possible to outline the strap and sternocleidomastoid muscles, which exhibit moderate vascularization in the optoacoustic image and have lower echogenicity as compared to the thyroid tissue. On the other hand, the left thyroid lobe is characterized by a homogenous echogenicity without pronounced vascularization.

The functional imaging capacity was further demonstrated via assessment of the blood oxygen state using multi-wavelength data acquisition. Maps of the spectrally-unmixed distributions of oxy- (HbO_2) and deoxy-hemoglobin (Hb) are shown in Fig. 2c and d, respectively. The images correctly assign the higher levels of HbO_2 signal to the common carotid artery, whereas the Hb signal appears more prominent in the subcutaneous microvasculature and the jugular vein.

The carotid vessels were further examined from the lower neck to the point of bifurcation using the second operation mode, focusing on evaluation of the blood flow. Four representative cross-sections from the color-Doppler scan are shown in Fig. 3. First, the common carotid artery (CCA) was visualized in transverse section at the base of the neck (Fig. 3a). To measure Doppler frequency shifts, the sampling window was centered at the CCA, as indicated by a blue rectangle in the image. As expected, the CCA shows a positive Doppler frequency shift (red). The probe was then rotated to acquire image of the CCA in its longitudinal section (Fig. 3b). The measured flow velocity of the common carotid artery was in the normal range between 30 and 40 cm/s [35] and no evidence of blood flow abnormalities were observed. The CCA was also scanned along its length in transverse section, reaching the bifurcation into the external (ECA) and internal (ICA) carotid arteries (Fig. 3c). Fig. 3d depicts longitudinal view of the carotid bifurcation showing ECA at the top and ICA at the bottom. The sampling window was placed in a superior region of the ECA and the ICA, where the flow is directed towards the transducer in both branches. Note that a proper alignment of the ultrasound beam parallel to the vector of

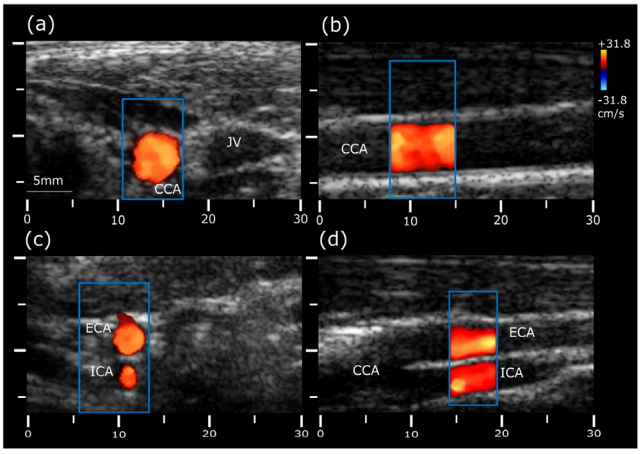

Fig. 3. Color Doppler measurements of blood velocity in the carotid arteries and jugular vein. (a) Transverse and (b) longitudinal views of the common carotid artery;. (c) Transverse and (d) longitudinal views of the carotid bifurcation into the external and internal carotid arteries. CCA: common carotid artery; ECA: external carotid artery; ICA: internal carotid artery; IJV: internal jugular vein.

blood flow is further limited by the need to maintain a reasonable light incidence angle onto the tissue surface for optimal MSOT image quality [20].

4. Discussion

Availability of new non-invasive and cost-effective imaging methods is crucial for facilitating accurate diagnosis and prevention of cardiovascular diseases. The showcased capability of mapping blood flow and oxygen state by means of the multi-segment detector array may provide a complementary diagnostic value to the existing functional imaging capacities of the stand-alone optoacoustic and ultrasound technologies. In our experiments, it was possible to clearly distinguish between the oxygenation status of structures located at depths of at least 1–2 cm, such as the carotid artery, the sternocleidomastoid muscles, the thyroid lobe and the jugular vein. The relevant imaging depth may yet vary among different individuals. The good imaging performance in the color Doppler measurements was made possible by the multi-segment probe design featuring a linear array segment compatible with standard implementations of Doppler technology used in the clinics [37,38].

Multi-modal functional imaging of the carotid artery bifurcation is of importance in the characterization of plaque development and stenosis, which are responsible for up to 25% of the ischemic strokes [36]. In combination with the rendered Doppler-based blood velocity measurements, the MSOT-based metrics may contribute to a more reliable assessment of the severity of carotid artery disease. Hemodynamic measurements are commonly done in patients undergoing surgery or in critical condition. In such cases, monitoring of multiple hemodynamic parameters may help in guiding treatments in a time frame that permits intervention to prevent organ failure [39]. The capacity for simultaneous mapping of multiple hemodynamic parameters is of utmost importance in the field of neuroimaging [40] where the complex mechanisms of neurovascular coupling cannot be fully characterized using functional magnetic resonance imaging (fMRI) [41,42] or Doppler US [43]. In addition to pure hemodynamic measurements, functional optoacoustic neuro-tomography has been recently shown capable of direct mapping of neuronal activity using calcium indicators [44].

Several technical aspects remained beyond the scope of the current work. For instance, quantification of oxygen saturation remains an active research area in MSOT due to inherent challenges with accurate estimation of wavelength-dependent light fluence in biological tissues [45]. In addition, the color Doppler measurements are usually angle-dependent, thus the angle formed between the interrogating sound beams and the blood flow must be optimized. The ideal case of 0° or 180° angle is generally hard to achieve when imaging randomly oriented vasculature [46], whereas angles exceeding 60° may introduce significant errors into the velocity calculation [47]. Therefore, implementation of beam steering capabilities to enable accurate Doppler imaging for broader range of angles is an important next step to consider. Note also that the optimal angle between the hand-held probe and the skin surface generally differs between the Doppler and MSOT imaging modes, thus an additional user training is necessary for achieving optimal scanning strategy.

In conclusion, the demonstrated feasibility for multi-modal MSOT, pulse-echo US and Doppler US imaging using the multi-segment detector array opens new perspectives for seamless multi-modal assessment of vascular function, and can potentially accelerate the translation of the optoacoustic technology into clinical practice.

Conflict of interest

Elena Merčep is employed by iThera Medical GmbH.

Funding

European Research Council Consolidator GrantERC-2015-CoG-682379.

References

[1] W.D. McArdle, F. Katch, V.L. Katch, Exercise Physiology: Energy, Nutrition, and Human Performance, 5th ed., Lippincott Williams and Wilkins, Philadelphia, 2001.
[2] B. Cauli, E. Hamel, Revisiting the role of neurons in neurovascular coupling, Front. Neuroenerg. 2 (2010), doi:http://dx.doi.org/10.3389/fnene.2010.00009.
[3] K. Tanishita, K. Yamamoto (Eds.), Vascular Engineering: New Prospects of Vascular Medicine and Biology with a Multidiscipline Approach, 1st ed. 2016 edition, Springer, Tokyo, 2016, pp. 2016.
[4] Doppler ultrasound: What is it used for? – Mayo Clinic, (n.d.). https://www.mayoclinic.org/doppler-ultrasound/expert-answers/faq-20058452 (accessed April 29, 2018).
[5] D. Razansky, N.C. Deliolanis, C. Vinegoni, V. Ntziachristos, Deep tissue optical and optoacoustic molecular imaging technologies for pre-clinical research and drug discovery, Curr. Pharm. Biotechnol. 13 (2012) 504–522.
[6] E. Herzog, A. Taruttis, N. Beziere, A.A. Lutich, D. Razansky, V. Ntziachristos, Optical imaging of cancer heterogeneity with multispectral optoacoustic tomography, Radiology 263 (2012) 461–468, doi:http://dx.doi.org/10.1148/radiol.11111646.
[7] I. Stoffels, S. Morscher, I. Helfrich, U. Hillen, J. Leyh, J. Lehy, N.C. Burton, T.C.P. Sardella, J. Claussen, T.D. Poeppel, H.S. Bachmann, A. Roesch, K. Griewank, D. Schadendorf, M. Gunzer, J. Klode, Metastatic status of sentinel lymph nodes in melanoma determined noninvasively with multispectral optoacoustic imaging, Sci. Transl. Med. 7 (2015), doi:http://dx.doi.org/10.1126/scitranslmed.aad1278 (317ra199).
[8] G.C. Langhout, D.J. Grootendorst, O.E. Nieweg, Wouters M.W.J.M, J.A. van der Hage, J. Jose, H. van Boven, W. Steenbergen, S. Manohar, T.J.M. Ruers, Detection of melanoma metastases in resected human lymph nodes by noninvasive multispectral photoacoustic imaging, Int. J. Biomed. Imaging 2014 (2014) 7, doi:http://dx.doi.org/10.1155/2014/163652 Article ID 163652.
[9] F. Knieling, C. Neufert, A. Hartmann, J. Claussen, A. Urich, C. Egger, M. Vetter, S. Fischer, L. Pfeifer, A. Hagel, C. Kielisch, R.S. Görtz, D. Wildner, M. Engel, J. Röther, W. Uter, J. Siebler, R. Atreya, W. Rascher, D. Strobel, M.F. Neurath, M.J. Waldner, Multispectral optoacoustic tomography for assessment of crohn's disease activity, N. Engl. J. Med. 376 (2017) 1292–1294, doi:http://dx.doi.org/10.1056/NEJMc1612455.
[10] X.L. Deán-Ben, T.F. Fehm, M. Gostic, D. Razansky, Volumetric hand-held optoacoustic angiography as a tool for real-time screening of dense breast,

J. Biophotonics 9 (2016) 253–259, doi:http://dx.doi.org/10.1002/jbio.201500008.
[11] A. Dima, V. Ntziachristos, In-vivo handheld optoacoustic tomography of the human thyroid, Photoacoustics 4 (2016) 65–69, doi:http://dx.doi.org/10.1016/j.pacs.2016.05.003.
[12] V.S. Dogra, B.K. Chinni, K.S. Valluru, J. Moalem, E.J. Giampoli, K. Evans, N.A. Rao, Preliminary results of ex vivo multispectral photoacoustic imaging in the management of thyroid cancer, AJR Am. J. Roentgenol. 202 (2014) W552–W558, doi:http://dx.doi.org/10.2214/AJR.13.11433.
[13] A. Taruttis, A.C. Timmermans, P.C. Wouters, M. Kacprowicz, G.M. van Dam, V. Ntziachristos, Optoacoustic imaging of human vasculature: feasibility by using a handheld probe, Radiology 281 (2016) 256–263, doi:http://dx.doi.org/10.1148/radiol.2016152160.
[14] A. Needles, A. Heinmiller, J. Sun, C. Theodoropoulos, D. Bates, D. Hirson, M. Yin, F.S. Foster, Development and initial application of a fully integrated photoacoustic micro-ultrasound system, IEEE Trans. Ultrason. Ferroelectr. Freq. Control. 60 (2013) 888–897, doi:http://dx.doi.org/10.1109/TUFFC.2013.2646.
[15] J.J. Niederhauser, M. Jaeger, R. Lemor, P. Weber, M. Frenz, Combined ultrasound and optoacoustic system for real-time high-contrast vascular imaging in vivo, IEEE Trans. Med. Imaging 24 (2005) 436–440, doi:http://dx.doi.org/10.1109/TMI.2004.843199.
[16] K. Daoudi, P.J. van den Berg, O. Rabot, A. Kohl, S. Tisserand, P. Brands, W. Steenbergen, Handheld probe integrating laser diode and ultrasound transducer array for ultrasound/photoacoustic dual modality imaging, Opt. Express 22 (2014) 26365–26374.
[17] J. Gateau, M.Á.A. Caballero, A. Dima, V. Ntziachristos, Three-dimensional optoacoustic tomography using a conventional ultrasound linear detector array: whole-body tomographic system for small animals, Med. Phys. 40 (2013) 013302, doi:http://dx.doi.org/10.1118/1.4770292.
[18] M. Oeri, W. Bost, N. Sénégond, S. Tretbar, M. Fournelle, Hybrid photoacoustic/ultrasound tomograph for real-time finger imaging, Ultrasound Med. Biol. 43 (2017) 2200–2212, doi:http://dx.doi.org/10.1016/j.ultrasmedbio.2017.05.015.
[19] X.L. Deán-Ben, E. Merčep, D. Razansky, Hybrid-array-based optoacoustic and ultrasound (OPUS) imaging of biological tissues, Appl. Phys. Lett. 110 (2017) 203703, doi:http://dx.doi.org/10.1063/1.4983462.
[20] E. Mercep, X.L. Dean-Ben, D. Razansky, Combined pulse-echo ultrasound and multispectral optoacoustic tomography with a multi-segment detector array, IEEE Trans. Med. Imaging 36 (2017) 2129–2137, doi:http://dx.doi.org/10.1109/TMI.2017.2706200.
[21] Allan L. Paul, Grant M. Baxter, Michael J. Weston, Clinical Ultrasound, 2-Volume Set: Expert Consult: Online and Print, Churchill Livingstone, Edinburgh, 2011.
[22] American National Standard for Safe Use of Lasers in Health Care Facilities, Standard Z136. 1–2000, (2007) . (Accessed 15 January 15 2017) https://www.lia.org/store/product/113.
[23] X.L. Deán-Ben, E. Bay, D. Razansky, Functional optoacoustic imaging of moving objects using microsecond-delay acquisition of multispectral three-dimensional tomographic data, Sci. Rep. 4 (2014) 5878, doi:http://dx.doi.org/10.1038/srep05878.
[24] S. Tzoumas, N. Deliolanis, S. Morscher, V. Ntziachristos, Unmixing molecular agents from absorbing tissue in multispectral optoacoustic tomography, IEEE Trans. Med. Imaging 33 (2014) 48–60, doi:http://dx.doi.org/10.1109/TMI.2013.2279994.
[25] M. Karaman, P.-C. Li, M. O'donnell, Synthetic aperture imaging for small scale systems, IEEE Trans. Ultrason. Ferroelectr. Freq. Control. 42 (1995) 429–442, doi:http://dx.doi.org/10.1109/58.384453.
[26] J.A. Jensen, Ultrasound imaging and its modeling, Imaging Complex Media Acoust. Seism. Waves, Springer, Berlin, Heidelber, 2002, pp. 135–166, doi:http://dx.doi.org/10.1007/3-540-44680-X_6.
[27] I. Trots, A. Nowicki, M. Lewandowski, Y. Tasinkevych, Synthetic Aperture Method in Ultrasound Imaging, (2011), doi:http://dx.doi.org/10.5772/15986.
[28] D. Maulik, Sonographic color flow mapping: basic principles, Doppler Ultrasound Obstet. Gynecol, Springer, Berlin, Heidelberg, 2005, pp. 69–84, doi:http://dx.doi.org/10.1007/3-540-28903-8_6.
[29] C.M. Otto, Textbook of Clinical Echocardiography, Elsevier, Saunders, 2009.
[30] K. Zell, J.I. Sperl, M.W. Vogel, R. Niessner, C. Haisch, Acoustical properties of selected tissue phantom materials for ultrasound imaging, Phys. Med. Biol. 52 (2007) N475–N484, doi:http://dx.doi.org/10.1088/0031-9155/52/20/N02.
[31] J.K. Oh, J.B. Seward, A.J. Tajik, The Echo Manual, 3rd ed., Lippincott Williams&Wilki, Philadelphia, 2006.
[32] E.K. Kerut, E.F. McIlwain, G.D. Plotnick, Handbook of Echo-Doppler Interpretation, John Wiley & Sons, 2008.
[33] H.R. Tahmasebpour, A.R. Buckley, P.L. Cooperberg, C.H. Fix, Sonographic examination of the carotid arteries, Radiographics 25 (2005) 1561–1575, doi:http://dx.doi.org/10.1148/rg.256045013.
[34] Workplace Safety Standards, (n.d.). https://webstore.ansi.org/(X(1))/safety-workplace/Default.aspx (accessed April 29, 2018).
[35] S. Kim, S. Lee, H.S. Choi, S.L. Jung, K.J. Ahn, B.S. Kim, Pseudostenosis at the origin of the vertebral artery on contrast-enhanced MRA: correlation with aortic motion on dynamic 3D time-Resolved contrast-Enhanced MRA, J. Korean Soc. Magn. Reson. Med. 16 (2012) 236–242, doi:http://dx.doi.org/10.13104/jksmrm.2012.16.3.236.
[36] W. Hacke, Cerebrovascular Ultrasound in Stroke Prevention and Treatment, 2 edition, Wiley-Blackwell, Chichester, West Sussex, 2011.
[37] J.E. Browne, A review of Doppler ultrasound quality assurance protocols and test devices, Phys. Medica PM Int. J. Devoted Appl. Phys. Med. Biol. Off. J. Ital. Assoc. Biomed. Phys. AIFB. 30 (2014) 742–751, doi:http://dx.doi.org/10.1016/j.ejmp.2014.08.003.
[38] F.A. Camfferman, G.M. Ecury-Goossen, J.E. La Roche, N. de Jong, W. van 't Leven, H.J. Vos, M.D. Verweij, K. Nasserinejad, F. Cools, P. Govaert, J. Dudink, Calibrating doppler imaging of preterm intracerebral circulation using a microvessel flow phantom, Front. Hum. Neurosci. 8 (2015), doi:http://dx.doi.org/10.3389/fnhum.2014.01068.
[39] J. Huygh, Y. Peeters, J. Bernards, M.L.N.G. Malbrain, Hemodynamic monitoring in the critically ill: an overview of current cardiac output monitoring methods, F1000Research 5 (2016) F1000, doi:http://dx.doi.org/10.12688/f1000research.8991.1.
[40] S. Gottschalk, T.F. Fehm, X.L. Deán-Ben, D. Razansky, Noninvasive real-time visualization of multiple cerebral hemodynamic parameters in whole mouse brains using five-dimensional optoacoustic tomography, J. Cereb. Blood Flow Metab. Off. J. Int. Soc. Cereb. Blood Flow Metab. 35 (2015) 531–535, doi:http://dx.doi.org/10.1038/jcbfm.2014.249.
[41] W.F. Eddy, M. Fitzgerald, C. Genovese, N. Lazar, A. Mockus, J. Welling, The challenge of functional magnetic resonance imaging, J. Comput. Graph. Stat. 8 (1999) 545–558, doi:http://dx.doi.org/10.2307/1390875.
[42] M.A. Silva, A.P. See, W.I. Essayed, A.J. Golby, Y. Tie, Challenges and techniques for presurgical brain mapping with functional MRI, NeuroImage Clin. 17 (2018) 794–803, doi:http://dx.doi.org/10.1016/j.nicl.2017.12.008.
[43] H. Lohmann, E.B. Ringelstein, S. Knecht, Functional transcranial doppler sonography, Front. Neurol. Neurosci. 21 (2006) 251–260, doi:http://dx.doi.org/10.1159/000092437.
[44] X.L. Deán-Ben, S. Gottschalk, G. Sela, S. Shoham, D. Razansky, Functional optoacoustic neuro-tomography of calcium fluxes in adult zebrafish brain in vivo, Opt. Lett. 42 (2017) 959–962.
[45] S. Tzoumas, A. Nunes, I. Olefir, S. Stangl, P. Symvoulidis, S. Glasl, C. Bayer, G. Multhoff, V. Ntziachristos, Eigenspectra optoacoustic tomography achieves quantitative blood oxygenation imaging deep in tissues, Nat. Commun. 7 (2016) 12121, doi:http://dx.doi.org/10.1038/ncomms12121.
[46] Top ten doppler errors and artifacts, Pegasus Lectures, (2011) . https://media.pegasuslectures.com/whitepapers/PegasusLectures_WhitePaper.pdf.
[47] F.R. Miele, Ultrasound Physics and Instrumentation, 4th edition, Pegasus Lectures, Inc., Forney, TX, 2006.

Elena Merčep is currently employed at iThera Medical as a senior R&D engineer, where she works on development and integration of algorithms for multispectral optoacoustic tomography and ultrasound imaging. She pursues a PhD on hybrid optoacoustic-ultrasound imaging under supervision of Prof. Daniel Razansky. Earlier she received Diploma in Biomedical Engineering from University of Electronic Technology in Moscow and MSc in Biomedical Computing from Technical University of Munich (2011–2013) with support of German Academic Exchange Service (DAAD).

Xosé Luís Deán-Ben received the diploma in automatics and electronics engineering from the Universidade de Vigo in 2004. He received the PhD degree from the same university in 2009. Since 2010, he serves as a research fellow at the Lab for Multi-Scale Functional and Molecular Imaging at the Institute for Biological and Medical Imaging (IBMI), Helmholtz Center Munich. His major research interests are the development of new optoacoustic systems for preclinical and clinical applications and the elaboration of mathematical algorithms for fast and accurate imaging performance.

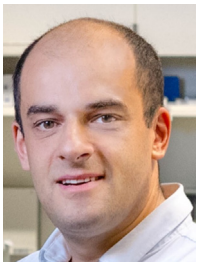

Daniel Razansky is Professor of Molecular Imaging Engineering at the Technical University of Munich and Helmholtz Center Munich, Germany. He earned degrees in Electrical and Biomedical Engineering from the Technion - Israel Institute of Technology and completed further training in bio-optics at the Harvard Medical School. His Lab pioneered a number of bio-imaging techniques successfully commercialized worldwide, among them the multi-spectral optoacoustic tomography (MSOT) and hybrid optoacoustic ultrasound (OPUS). Prof. Razansky is a Fellow of the Optical Society of America and serves on the editorial boards of several journals published by Springer Nature, Elsevier, IEEE and AAPM.